Corrosion Science 128 (2017) 213–223

Contents lists available at ScienceDirect

Corrosion Science

journal homepage: www.elsevier.com/locate/corsci

The corrosion of $Zr(Fe, Cr)_2$ and Zr_2Fe secondary phase particles in Zircaloy-4 under 350 °C pressurised water conditions

Kirsty Annand[a,*], Magnus Nord[a], Ian MacLaren[a], Mhairi Gass[b]

[a] Materials and Condensed Matter Physics, School of Physics and Astronomy, University of Glasgow, Glasgow G12 8QQ, UK
[b] AMEC Foster Wheeler, Clean Energy, Walton House, Birchwood Park, WA3 6GA, UK

ARTICLE INFO

Keywords:
Oxidation
SPPs
Zircaloy-4
STEM
DualEELS

ABSTRACT

Using Scanning Transmission Electron Microscopy (STEM) coupled with Dual Electron Energy Loss Spectroscopy (DualEELS) and scanned diffraction, the corrosion and incorporation of Secondary Phase Particles (SPPs) in the oxide layer of Zircaloy-4 material has been investigated. This study focuses on mapping the corrosion of Zr_2Fe and $Zr(Fe, Cr)_2$ precipitates during the oxidation process and depicting their morphology as the oxidation front advances through the material. It has been found that Zr_2Fe SPPs retain the same general shape as in their pre oxidation stage, and transform to a nanocrystalline homogeneous mixed oxide, with a strong crystallographic texture, but hitherto unknown structure. The $Zr(Fe, Cr)_2$ Laves-phase SPPs however, oxidise in a notably more complicated manner. As the α-Zr around an SPP begins to oxidise, the SPP is completely encapsulated by the ZrO_2 whilst much of the SPP remains initially unoxidised. But, on oxidation, significant elemental segregation takes place, usually leaving a Cr_2O_3-rich cap, a nanocrystalline Zr,Cr mixed oxide body and veins of well-crystallised metallic iron. Both forms of SPP have a different expansion on oxidation compared to the Zr, resulting in cracking of the ZrO_2.

1. Introduction

Worldwide, Zircaloy-4 (Zr-1.5%Sn-0.2%Fe-0.1%Cr) has been a popular material of choice for the containment of nuclear fuel and other structural components within commercial Pressurised Water Reactors (PWRs), due to their high corrosion resistance [1], low thermal neutron cross section [2], superior mechanical properties, and favourable chemical stability in highly aggressive environments. However, waterside corrosion of these cladding materials results in the creation of an oxide layer on the surface of the metal, resulting in degradation of their integrity over time. It is well established that the corrosion process of zirconium base alloys is a multifaceted one, characterised by an initial, rapid formation of a thin oxide layer on the surface of the material; followed by a decreased oxidation rate which follows the square or cube root of time [1,3], up until 2–4 μm of oxide has grown on the surface of the metal. Following this, a kinetic transition occurs and the oxidation proceeds more rapidly again. This process is periodic, and may be repeated several times, until the oxide thickness grows almost linearly with time [1]. A number of recent studies have elucidated the nanoscale details of this process in the alpha-Zr phase in the Zircaloy [4–6]. In this case, with the addition of alloying elements such as Sn, Fe and Cr to the Zr base metal, up to a value of about 2 wt.%, the corrosion behaviour of the alloy becomes more predictable and less likely to suffer catastrophic breakaway corrosion. The Fe and Cr alloying elements are shown to have a solubility of < 150 wt. ppm in Zr-1.4% Sn [7], and 290 wt. ppm [8] in Zircaloy-4. Therefore, much of the content of these elements precipitate during the alpha-phase annealing as intermetallic-Zr compounds, which sit as precipitates within the base metal [1]. It should be noted that improved corrosion resistance with the addition of alloying elements is not always the case, such as is seen in some binary alloy systems. Although the addition of Cr to a Zr base alloy improves the alloy's resistance to oxidation [9], this improvement is offset by the fact that the introduction of $ZrCr_2$ laves phase precipitates to the matrix can result in embrittlement of the material [9]. In the Zr-Fe alloy system, the laves C15-Fe_2Zr phase is found to be the most stable phase [10], although others (such as c-$FeZr_2$), relatively less so [10]. Precipitates in the Zr1%Fe system have also been seen to show an increased oxidation rate when in contact with the gas:oxide surface [11].

There are two primary types of SPP which are found within Zircaloy alloy series, namely $Zr_2(Ni, Fe)$ and $Zr(Fe, Cr)_2$ type precipitates. The former is an intermetallic C16 phase (isostructural with $CuAl_2$), frequently seen in Zircaloy-2 [12–15], whereas the latter mostly appears as an hexagonal intermetallic Laves phase with the C14 structure, and is seen frequently in both Zircaloy-2 and -4 [12,13,15–20].

* Corresponding author.
E-mail address: k.annand.1@research.gla.ac.uk (K. Annand).

http://dx.doi.org/10.1016/j.corsci.2017.09.014
Received 6 January 2017; Received in revised form 1 September 2017; Accepted 11 September 2017
Available online 13 September 2017
0010-938X/ © 2017 The Authors. Published by Elsevier Ltd. This is an open access article under the CC BY license (http://creativecommons.org/licenses/BY/4.0/).

Early work by Chemelle et al. [12] aimed to investigate the morphology and composition of SPPs in Zircaloy-2, using transmission electron microscopy (TEM). They found that all precipitates were either nickel-bearing with a tetragonal Zr_2Ni-type phase (where Ni is partly replaced by Fe), or chromium-bearing with a hexagonal $ZrCr_2$-type phase (where Cr is partly replaced by Fe). No iron-zirconium particles were detected. Later, Charquet [7] found that an increased iron content resulted in Zircaloy-4 having a better resistance to corrosion under steam conditions. However, the results reveal that in a Zr-1.4% Sn matrix, adding Fe in an amount equivalent to the (Fe + Cr) content in Zircaloy-4 is less effective than the simultaneous addition of Fe and Cr. Therefore, it was decided to study the influence of the Fe/Cr ratio in Zircaloy-4 material. It was deduced that the optimum corrosion resistance is obtained for Fe/Cr ratios in the range from 1.5 to 5. They noted that, for ratios less than 4, the only precipitates observed correspond to the $Zr(Fe, Cr)_2$ phase, in which the proportions of iron and chromium are comparable to their nominal concentrations. Moreover, for larger Fe/Cr ratios, further phases of the type Zr_2Fe and Zr_3Fe were found, highlighting that the substitution of Cr by Fe in $ZrCr_2$ is limited.

In order to better understand these SPPs, Meng et al. [13] then analysed them in Zircaloy-2 using TEM and energy dispersive X-ray spectroscopy (EDS). The most common were the $Zr_2(Fe,Ni)$-type which exhibited two size ranges, the larger ones being found at the α-Zr grain boundaries. They had a composition of $Zr_2(Fe_{0.4\text{-}0.5}Ni_{0.6\text{-}0.5})$, and a body-centred tetragonal structure, as expected for this composition. The smaller of these particles were found to be generally smaller than 1 μm and had an elliptical shape. The second SPP type found was the hexagonal $Zr(Fe, Cr)_2$ Laves phase with a composition of $Zr(Cr_{0.55\text{-}0.57}Fe_{0.45\text{-}0.43})_2$. These particles had a size similar to the smaller (< 1 μm) $Zr_2(Fe, Ni)$-type precipitates and exhibited the expected hexagonal C14 structure. These $Zr(Fe,Cr)_2$ SPPs were also regularly found to contain parallel stacking-faults. It should be noted that an SPP size of 1 μm is around 5 times larger than what would be expected in the largest SPPs in industrial alloys (of the order to 100–200 nm). As Zircaloy-2 has a different composition to Zircaloy-4, the corrosion resistance will differ between alloys, and thus, this reference may not be entirely adequate for comparison between SPP size in work by Meng et al. [13], and the current study.

Literature suggests that the oxidation process is considerably altered when factors such as distribution, size and chemical composition of the $Zr(Fe, Cr)_2$ intermetallic precipitates in Zircaloy-2 and Zircaloy-4 and $Zr_2(Fe,Ni)$ particles in Zircaloy-2 [17], are varied. However, there are still many outstanding questions about the exact mechanisms by which the oxidation of SPPs takes place. It is understood that the corrosion resistance of the alloy is strongly dependant on microstructure with the composition, size and volume fraction of SPPs being of particular importance. Optimal balance of these properties allows for fine control of life-limiting properties of the alloy such as corrosion resistance, hydrogen pick up and grain size [21]. In particular, it has been noted that favourable nodular corrosion resistance requires fine precipitates [22], whereas a certain minimum particle size is necessary for satisfactory uniform corrosion behaviour [23].

The oxidation of the Laves phase precipitates has been studied previously using conventional TEM and spot analysis with EDS. Pêcheur et al. [17] showed after oxidation in steam at 400 °C that such precipitates in Zircaloy 4 are often oxidised after the surrounding Zr matrix is oxidised to ZrO_2, that some diffraction patterns from oxidised SPPs could be consistent with a tetragonal ZrO_2 phase, and that some iron was redistributed as bcc metallic iron within the oxidised particles. De Gabory *et al.* [20] also recently concluded that the oxidation of such C14 Laves phase precipitates results in nanocrystalline areas with a large phase content of tetragonal ZrO_2. Pêcheur [24] studied the oxidation of similar precipitates in Zircaloy-4 in superheated lithiated water. They found that it is not until ~300 nm from the metal-oxide interface that SPPs begin to oxidise, and iron depletion is observed. It is suggested that due to the dissolution of iron from the precipitates to the surrounding zirconia matrix at this point, the alloying elements can modify the inner oxide grain properties, such as stabilising the tetragonal ZrO_2 phase.

There are also reports in Zr-1%Fe alloys of iron oxide precipitates in the oxide [11], although their structure was not determined, and there was no quantification of their exact composition. There are, however, very few observations of Zr_2Fe precipitates in Zircaloy-4 [25] and no known studies of the oxidation of such particles.

The current work is a systematic study of the structure and chemistry of SPPs in Zircaloy-4 after corrosion in pressurised water at 360 °C covering both Zr_2Fe and $Zr(Fe, Cr)_2$ type precipitates. Specifically, mapping of the chemistry using electron energy loss spectroscopy (EELS) spectrum imaging using DualEELS is used to produce spatially resolved quantitative maps of elemental content with few nanometre resolution elucidating in detail the oxidation process. This is combined with scanned diffraction to elucidate the crystallographic structure within these nanocrystalline oxidised SPPs. It is shown that whilst the oxidation of Zr_2Fe is relatively straightforward, the oxidation of the Laves phase precipitates is highly complex resulting in segregation into bands of a mixed Cr-Zr oxide and well-crystallised α-Fe.

2. Experimental methods

2.1. Materials and corrosion

All samples were prepared and corroded by Amec Foster Wheeler. The material of interest is standard recrystallised annealed (RXA) Zircaloy-4 (Zr-1.5%Sn-0.2%Fe-0.1%Cr). Samples were mechanically polished to remove surface scratches before being pickled in an HF solution to remove 50 μm of material from all surfaces. The samples were then exposed to pressurised water at 180 bar and 350 °C with a room temperature pH of 10 for various durations to simulate PWR in-reactor conditions [26,27]. The average dissolved hydrogen content was measured to be 3.65 ppm using a calibrated hydrogen orbisphere. Oxide thicknesses were average thicknesses, as inferred from weight gain measurements using the relationship 15 mg/dm2 = 1 μm.

2.2. Microscopy

Using a FEI Nova Nanolab instrument, samples were lifted out as cross sections through the oxide. Protection of the sample surface was done using electron beam, and then ion beam deposited platinum before initial thinning with 30 kV Gallium ions was performed. Samples were then lifted out and attached to suitable copper support grids with platinum, and final thinning was performed using lower energy Ga beams down to 5 kV.

Scanning transmission electron microscopy (STEM) and EELS-spectrum imaging (EELS-SI) using a probe corrected JEOL ARM200F (cold FEG) with a GIF Quantum ER electron energy loss spectrometer with DualEELS functionality. Typically, a probe semiconvergence angle of 29 mrad was employed for EELS-SI acquisition and a post-specimen lens setup that gave a spectrometer acceptance angle of 36 ± 0.4 mrad. Step sizes for EELS-SI were typically a few nm.

In order to determine crystallographic information of the particles, scanned diffraction was performed with the same instrument using aberration-corrected Lorentz-mode (i.e. objective lens switched off, and the probe formed using the condenser lenses and the aberration corrector, with a small convergence angle) [28]. Acquisition of the scanned diffraction datasets was controlled using the Diffraction Imaging plug-in for Spectrum Imaging within Gatan Digital Micrograph. Datasets for Zr_2Fe and $Zr(Fe, Cr)_2$-type SPPs in the oxide were acquired using the 30 μm condenser lens aperture which gives a convergence angle of 1.5 mrad and a diffraction-limited probe size of ~0.8 nm, a 40 cm camera length to give the appropriate size of diffraction pattern on the Gatan Orius CCD camera, and a 0.5 s exposure time per pixel for the $Zr(Fe, Cr)_2$ dataset, and a 0.2 s exposure time per pixel for the Zr_2Fe dataset.

All phases were calibrated on the assumption that the matrix of the bulk material was primarily monoclinic ZrO_2, as consistent with Garner et al. [5] and many other studies.

2.3. EELS data analysis

Post-acquisition, datasets were processed using a sequence of steps, all performed within Gatan Digital Micrograph (version 2.3), in order to separate the real spectroscopic signals from artefacts and noise, and to quantify the resulting datasets. Full details of these post-processing steps can be found at [29,30].

Digital Micrograph quotes a cross sectional error of 25% for an M shell, 10% for an L shell and 5% for a K shell. This is due to the fact that in general, the error in the K shell can be calculated from hydrogenic calculations, and so can be calculated to high accuracy. The L shell however, contains more quantum effects, and as there is more splitting of sub shells, this calculation is not so simple, and a 10% error is quoted. The M shell is more complicated again as the cross section error is calculated by the number of electrons involved, and so is quoted as 25%. This is most likely too high. More detailed analysis of the accuracy of these calculations is included in Egerton [31]. Errors in this work were originally calculated on this basis, however, it should be noted that for two neighbouring elements with the same edge, the error in the absolute cross section will be similar in magnitude and direction in most cases [31], causing the systematic errors to mostly cancel each other out.

Random statistical errors were also analysed according to Poisson statistics. However, due to our setup where hundreds or thousands of spectra are collected for every SPP, the statistics are so good that the fractional random error $1/\sqrt{N}$ is negligible. So, it is concluded that the primary component of the error arises from the uncertainty in where the background and signal window is set in Digital Micrograph. In order to calculate this, the width, and onset energy of the background and signal windows were altered slightly several times, in order to determine the average difference in the cross sections due to several window alterations. An average error of better than 5 at.% was found in all cases, and is quoted as the general error of all elemental quantifications.

All images shown are oriented so that the vertical direction upwards is towards the outer surface of the oxide scale, and the vertical direction downwards is towards the metal bulk.

3. Results

This study has focussed on the morphology and chemical composition of both Zr_2Fe and $Zr(Fe, Cr)_2$ SPPs found within samples of Zircaloy-4, as the oxidation front advances through the metal matrix. Particular attention was paid to mapping the particles both pre-, and post- oxidation. However, there are a few instances where the $Zr(Fe, Cr)_2$ particles are seen to sit right at the metal-oxide interface, just undergoing, or having just undergone oxidation. Special mention will be made of these instances in Section 3.4 when discussing the corrosion of these binary particles.

3.1. Zr_2Fe SPP in metal

Whilst Zr_2Fe SPPs have rarely been reported in the literature, in the work of which this publication forms a part, more than 30 different Zircaloy-4 specimens have been prepared and analysed and Zr_2Fe-type precipitates have been observed on multiple occasions (even if they are still rarer than Laves phase SPPs). Fig. 1 shows elemental maps of Zr and Fe of one such particle within the unoxidised metal, together with a background-subtracted EEL spectrum covering the range from 500 to 800 eV (which includes oxygen-K and iron-$L_{2,3}$ edges). This specimen has an oxide thickness of 4.05 μm and thus, is a post transition specimen. The SPP is located ~3 μm below the metal oxide interface.

Quantification of this high-loss data has shown that there is no detectable chromium content within this particle, as can be seen in the EEL spectrum in Fig. 1c, where the white lines of Cr above 575 eV are notably absent. The absolute composition of the particle is shown in Table 1 below and this is fully consistent with the idealised Zr_2Fe stoicheometry.

3.2. Zr_2Fe SPP in oxide

As the oxidation front continues to advance through the α-Zr, secondary phase particles meeting this interface will be subject to corrosion. The oxidation front will proceed to oxidise the SPP and the surrounding material, leaving behind an oxidised SPP stranded in the oxide layer. EEL mapping, HAADF imaging, and scanned diffraction of one such oxidised Zr_2Fe SPP are shown in Fig. 2. This post transition specimen has an oxide thickness of 4.72 μm, with the SPP found 3 μm above the metal:oxide interface.

It is clear that the core of the oxidised SPP is rich in iron, as seen in Fig. 2a, but there is little evidence of any strong internal segregation of the iron – the variation of intensity in the iron map from centre to edge in the SPP is due to this being a ~100 nm precipitate fully embedded in a thin section thicker than this. Just quantifying the composition using the region of the energy loss spectrum shown in Fig. 2e covering the O-K and Fe-$L_{2,3}$ edges results in the composition shown in Table 2. The calculated composition was achieved by doing some simple balancing of equations, based on the assumption that an ideally stoichiometric Zr_2Fe particle oxidises to a mixture of Fe_2O_3 and ZrO_2. The measured composition lies within one standard deviation of the calculated composition giving us confidence that this assumption of full oxidation to Fe^{3+} and Zr^{4+} is likely.

A very small chromium-rich region can be seen at the edge of the SPP in Fig. 2b. Whether this arose from a separate Cr-containing SPP on the edge of the Zr_2Fe SPP, or from a small amount of Cr in the Zr_2Fe is not clear.

An HAADF image of another oxidised Zr_2Fe is shown in Fig. 2c. This shows a very fine, apparently nanocrystalline structure. Additionally, it appears to have expanded in the oxidation direction, but also seems to be associated with a crack in the neighbouring ZrO_2. This suggests that the expansion on oxidation for this phase and the Zr are different, leading to such cracking effects.

Fig. 2d shows a typical diffraction pattern from a scanned nanodiffraction dataset from the SPP also shown in Fig. 2a. The same diffraction pattern was seen across the particle, but with frequent small rotations of the spot pattern. Even in this pattern, whilst it is clear that it corresponds to a zone axis pattern, there are arcs of several spots for each reflection. Thus, the nanocrystallites that comprise the particle display a very strong crystallographic texture. The pattern shown could correspond to a ⟨114⟩ pattern of a cubic structure of lattice parameter 4.7 Å, and such an indexing is included on the pattern. This is unexpected, since iron doping of ZrO_2, whilst it stabilises tetragonal [32], and possibly cubic phases [33], has previously only been shown to result in lattice parameters down to 5.034 Å for $Zr_{0.6}Fe_{0.4}O_y$ [33]. Conversely, this would also not be explained by the formation of magnetite Fe_3O_4 or maghemite Fe_2O_3 (cubic spinels with lattice parameters 8.35–8.4 Å [half the lattice parameter would be ~4.2 Å]). It is possible that this is a metastable hydrated phase formed at these low temperatures in superheated water and which bridges the lattice parameter gap between ~4.2 and ~5 Å for iron oxide and zirconia, but this is uncertain at this point and requires further investigation.

3.3. $Zr(Fe, Cr)_2$ SPP in metal

As expected, $Zr(Fe, Cr)_2$ precipitates were commonly observed in the metal matrix. Fig. 3 is acquired from a post transition specimen which has an oxide layer of 4.05 μm and depicts two such $Zr(Fe, Cr)_2$ SPPs located 2.8 μm from the metal:oxide interface. These SPPs

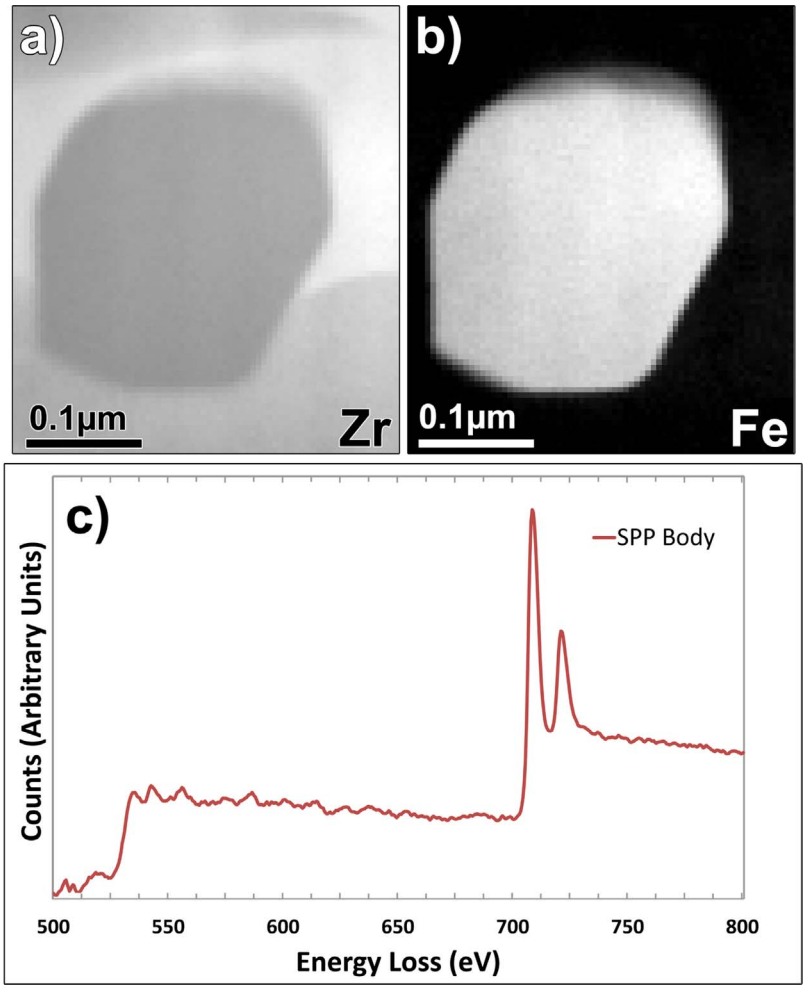

Fig. 1. EELS spectrum imaging of a Zr_2Fe SPP in the unoxidised metal, about 3 µm below the metal:oxide interface: a) map of zirconium areal density; b) map of iron areal density; c) EEL spectrum showing iron-$L_{2,3}$ edges at 721 and 708 eV respectively which depict a high Fe content within the SPP. The SPP contains no detectable Cr, as shown by the lack of the chromium-$L_{2,3}$ edges at 584 and 575 eV respectively.

Table 1
Chemical composition of a typical Zr_2Fe particle found in the metal as determined by EELS analysis.

Element	Composition (at.%)
Zr ($M_{4,5}$ edge)	62 ± 5
Fe ($L_{2,3}$ edge)	38 ± 5

together, have an average diameter of 0.3–0.35 µm and are not uniform in shape, but have a very definite, faceted outline. The size of these precipitates are consistent with the size of Zr_2(Fe, Ni) precipitates found in Zircaloy-2 by Meng et al. [13] (< 1 µm), with a Fe/Cr ratio of 0.83. Whilst both Cr and Fe are found throughout, it should be noted that there is also some evidence of a Fe concentration within the centre of one precipitate. It may also be noted that there is a clear O enrichment at the edges of the SPPs, over and above the slight surface oxidation on the FIB-prepared specimen. It may be that some of the Cr or Zr in such particles reacts with any dissolved oxygen in the alpha-Zr matrix to form a thin surface oxide layer on such particles. Integrating the spectra from much of the particles and quantifying the edges yields the bulk composition shown in Table 3. This is very much as expected for Zr(Fe, $Cr)_2$.

3.4. *Zr(Fe, $Cr)_2$ SPP at metal-oxide interface (during oxidation)*

As the oxidation front advances into the metal, particles are seen which are in the process of being oxidised. It is expected on the basis of electronegativity values that the first constituent to oxidise will be the zirconium, followed by chromium and finally iron: Zr has an electronegativity of 1.33, Cr 1.66 and Fe 1.83. As shown below, this is consistent with the observations in this work

Fig. 4 shows an oxidised cluster of SPPs just inside the ZrO_2 scale, so the oxidation front had just moved past these precipitates when the sample was removed from the autoclave and prepared for STEM analysis. This post transition specimen has an oxide thickness of 2.96 µm as calculated from weight gain measurements, and is located in the oxide, just at the oxide:metal interface. Overall, the majority of the particles are clearly rich in Cr and appears to be the Zr(Fe, $Cr)_2$ type which has/have been at least partially oxidised. Whilst Fe is found throughout, it is clearly segregated strongly to bands within the particle. There is Cr throughout much of the particle, but there are some particularly rich areas at points. Wherever Cr is rich, there is also plenty of Zr (although naturally much less than in the pure ZrO_2 matrix surrounding). The oxygen map shows that the Fe-rich veins are very low in O, and also the areas closest to the unoxidised metal are very low in oxygen. A crack is observed intersecting with the particle to the top right, especially visible in this oxygen map, as previously also noted for the oxidation of Zr_2Fe.

Integrating the spectra from much of the two Zr(Fe, $Cr)_2$ particles and quantifying the edges yields the bulk composition shown in Table 4. This is reasonably consistent with the bulk cation composition for an unoxidised particle shown in Table 3, although a little high in Zr, however, there may have been some ZrO_2 matrix overlapped with the edges of the SPP. The oxygen: metal content is only 1:1, rather than 3:2 for Cr oxide or 2:1 for Zr oxide, suggesting that this particle is nowhere near totally oxidised.

Four regions highlighted in Fig. 4e have been selected, and their

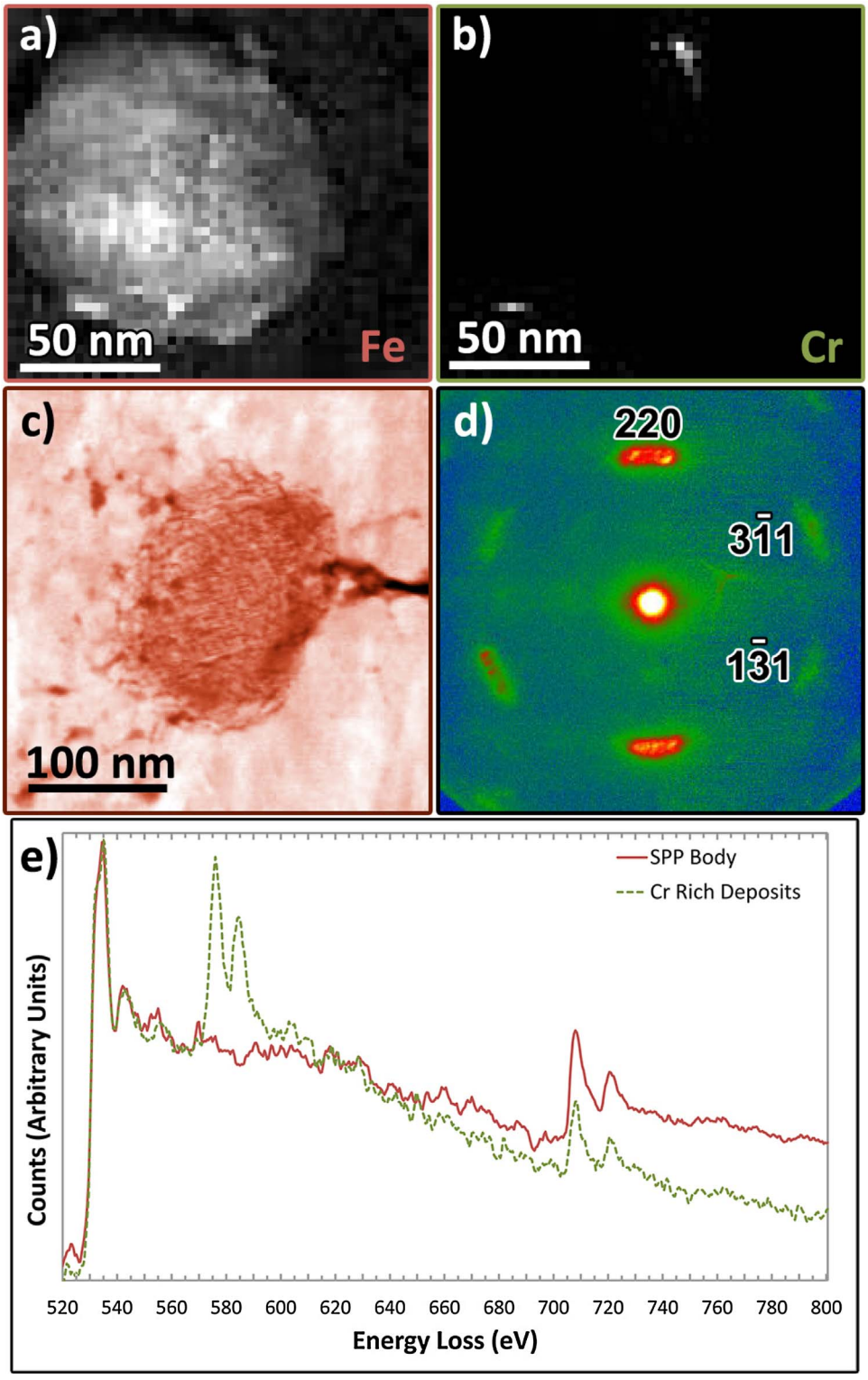

Fig. 2. EELS spectrum imaging of a Zr_2Fe SPP stranded in the oxide post corrosion: a) map of iron areal density: b) map of chromium areal density; c) a false coloured HAADF image of a different oxidised Zr_2Fe SPP showing the nanostructured nature of particle; d) a diffraction pattern from a scanned diffraction experiment on the SPP shown in a), a tentative indexing on the basis of a face centred cubic unit cell is included; e) an EEL spectrum showing the SPP body (red) and areas of Cr deposits (green). (For interpretation of the references to colour in this figure legend, the reader is referred to the web version of this article.)

Table 2
Chemical composition of a typical oxidised Zr_2Fe particle as determined by EELS analysis.

Element	Measured Composition (at.%)	Stoichemetric Composition (at.%)
O (K edge)	87 ± 5	84.6
Fe ($L_{2,3}$ edge)	13 ± 5	15.4

low- and high-loss EEL spectra shown in Fig. 4f and g respectively.

The region at the bottom centre of the oxidised SPP highlighted with a blue dot in Fig. 4e is unlike most parts of the SPP and shows almost no Cr, and low Fe content compared to the rest of the oxidised SPP. The low-loss which represents this (region 1 in Fig. 4f) shows a three peaked spectral signature, typical of an oxide (the highest peak being associated with the $N_{2,3}$ edge of Zr). The high-loss spectrum for this area (region 1 in Fig. 4g) confirms the oxidation of this area showing a strong peak of oxygen at 532 eV. The Fe $L_{2,3}$ edge is also present,

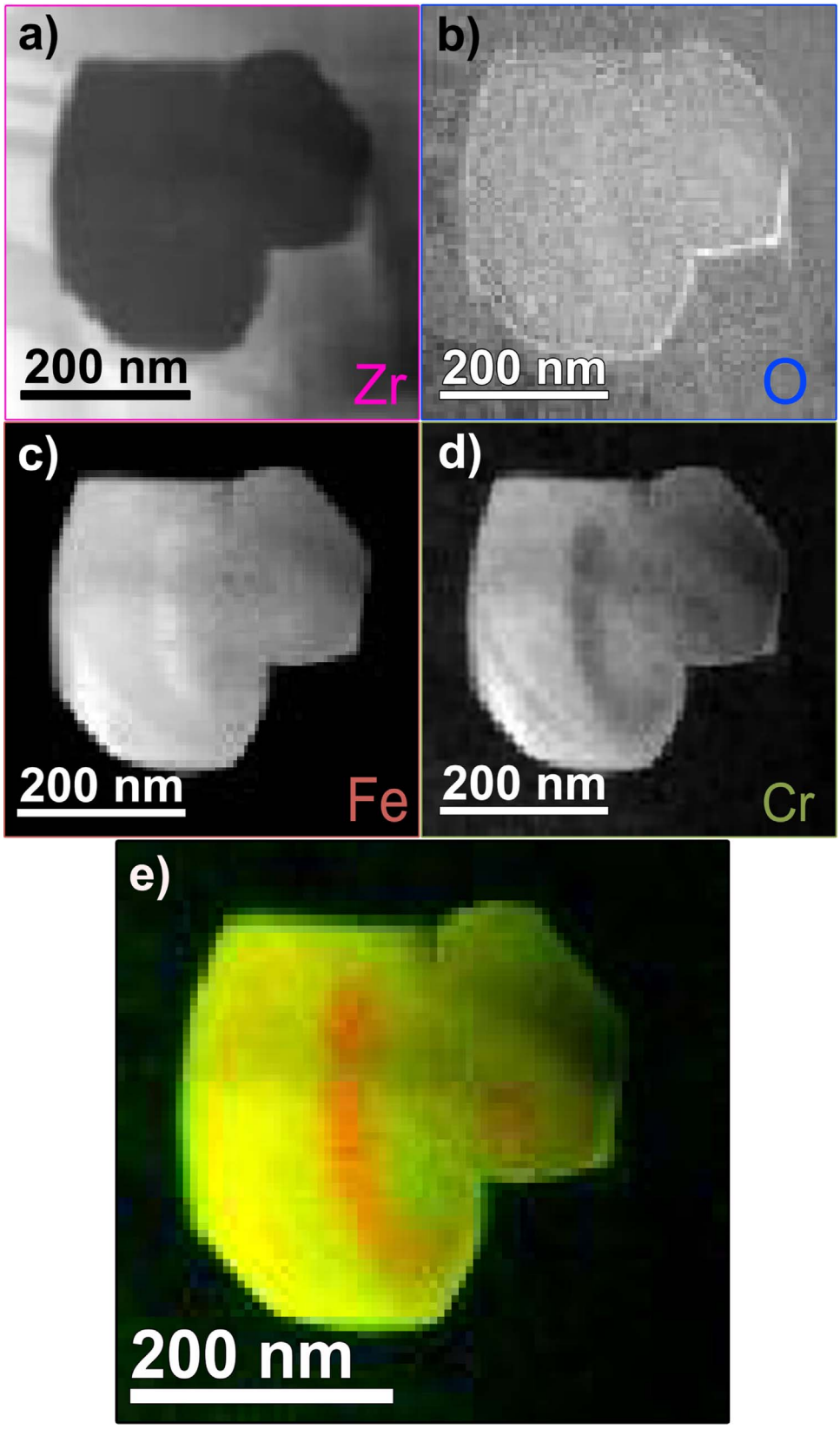

Fig. 3. High-loss quantification of $Zr(Fe, Cr)_2$ SPP: a) map of zirconium areal density: b) map of oxygen areal density; c) map of iron areal density; d) map of chromium areal density; and e) false colour RGB composite of SPP where green = Cr and red = Fe. (For interpretation of the references to colour in this figure legend, the reader is referred to the web version of this article.)

however, there is no detectable Cr within this area of the SPP. This leads to the assumption that this area is an oxidised small Zr_2Fe precipitate, which was originally neighbouring a cluster of $Zr(Fe, Cr)_2$ SPPs prior to oxidation.

The orange dot in Fig. 4e highlights one of the Fe-rich veins in the SPP, and low- and high-loss spectra are shown as region 2 in Fig. 4f and g. The low-loss EEL spectrum has just a single plasmon peak at about 25 eV, entirely consistent with a metal (and in a similar to position to that for pure iron [34]). The high-loss signature for this area confirms that there is minimal oxygen content over and above surface oxide in

Table 3
Chemical composition of a typical unoxidised $Zr(Fe, Cr)_2$ particle as determined by EELS analysis.

Element	Composition (at.%)
Zr ($M_{4,5}$ edge)	34.6 ± 5
Fe ($L_{2,3}$ edge)	40.7 ± 5
Cr ($L_{2,3}$ edge)	24.7 ± 5

Table 4
Chemical composition of a typical oxidised $Zr(Fe, Cr)_2$ particle as determined by EELS analysis.

Element	Composition (at.%)
Zr ($M_{4,5}$ edge)	19.7 ± 5
O (K edge)	50.2 ± 5
Fe ($L_{2,3}$ edge)	19.1 ± 5
Cr ($L_{2,3}$ edge)	11.1 ± 5

this area, as well as little Cr content. As Fe is the final constituent to oxidise according to the electronegativity argument presented above, it appears that the Cr and Zr have monopolised the oxygen supply during corrosion resulting in the segregation of separate veins of metallic iron. The fact that many of these bands run perpendicular to the corrosion direction suggest that Fe is rejected by the growing oxide until it builds up into a sufficient concentration to precipitate separately, and that this process repeats itself multiple times in oxidisation of such an SPP. This particular vein, however, runs at an angle to the growth direction, and it is speculated that this could have originally marked the boundary between two neighbouring $Zr(Fe, Cr)_2$ SPPs.

Much of the SPP is dominated by the mixed, Cr, Zr oxide. Representative spectra of this phase are taken from the area highlighted in Fig. 4e in purple and shown as region 3 in Fig. 4f and g. As for other oxide areas, a 3-peak structure is seen in the low-loss. Here, the high-loss spectrum demonstrates an oxidised region containing Cr, some Fe (and some Zr, not shown in this spectrum)

An area on the tip of the SPP is highlighted with a green dot in Fig. 4e with spectra shown as region 4 in Fig. 4f and g, whose low-loss EEL spectrum shows a composition somewhere between the oxidised regions 1 and 3, and the Fe-rich metallic region 2. The high-loss spectrum is principally chromium oxide, with little Fe. This is consistent with Cr being one of the first constituents to oxidise, resulting in a Cr rich SPP tip (since this area would have been the first region of the SPP to come into contact with the metal-oxide interface).

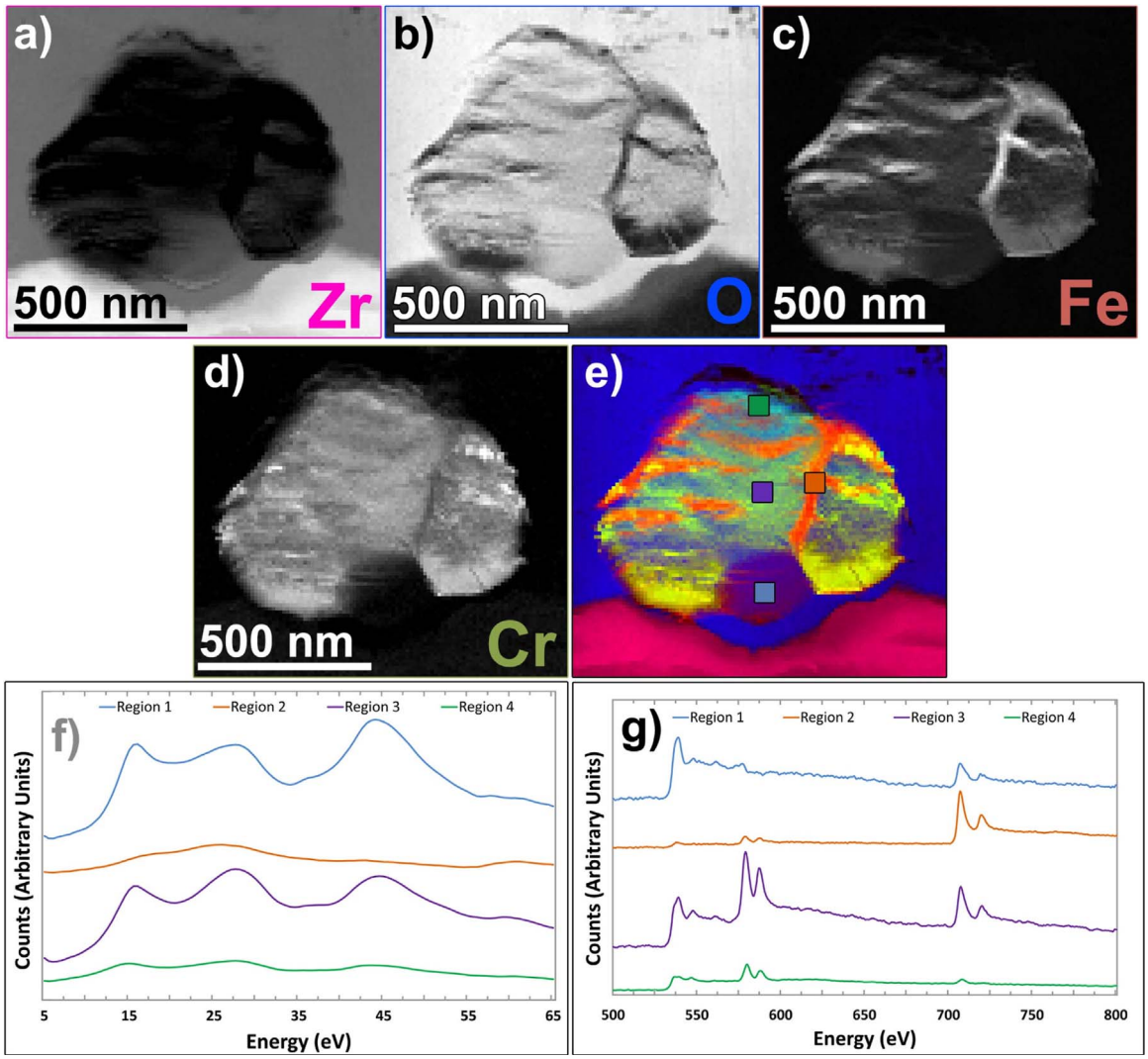

Fig. 4. High-loss quantification of a $Zr(Fe, Cr)_2$ precipitate at the oxidation front showing: a) map of zirconium areal density; b) map of oxygen areal density; c) map of iron areal density; d) map of chromium areal density; e) RGB composite of all phases where pink = Zr, blue = O, red = Fe and green = Cr, with 3 areas highlighted and their corresponding; f) low-loss and; g) high-loss spectral signatures. (For interpretation of the references to colour in this figure legend, the reader is referred to the web version of this article.)

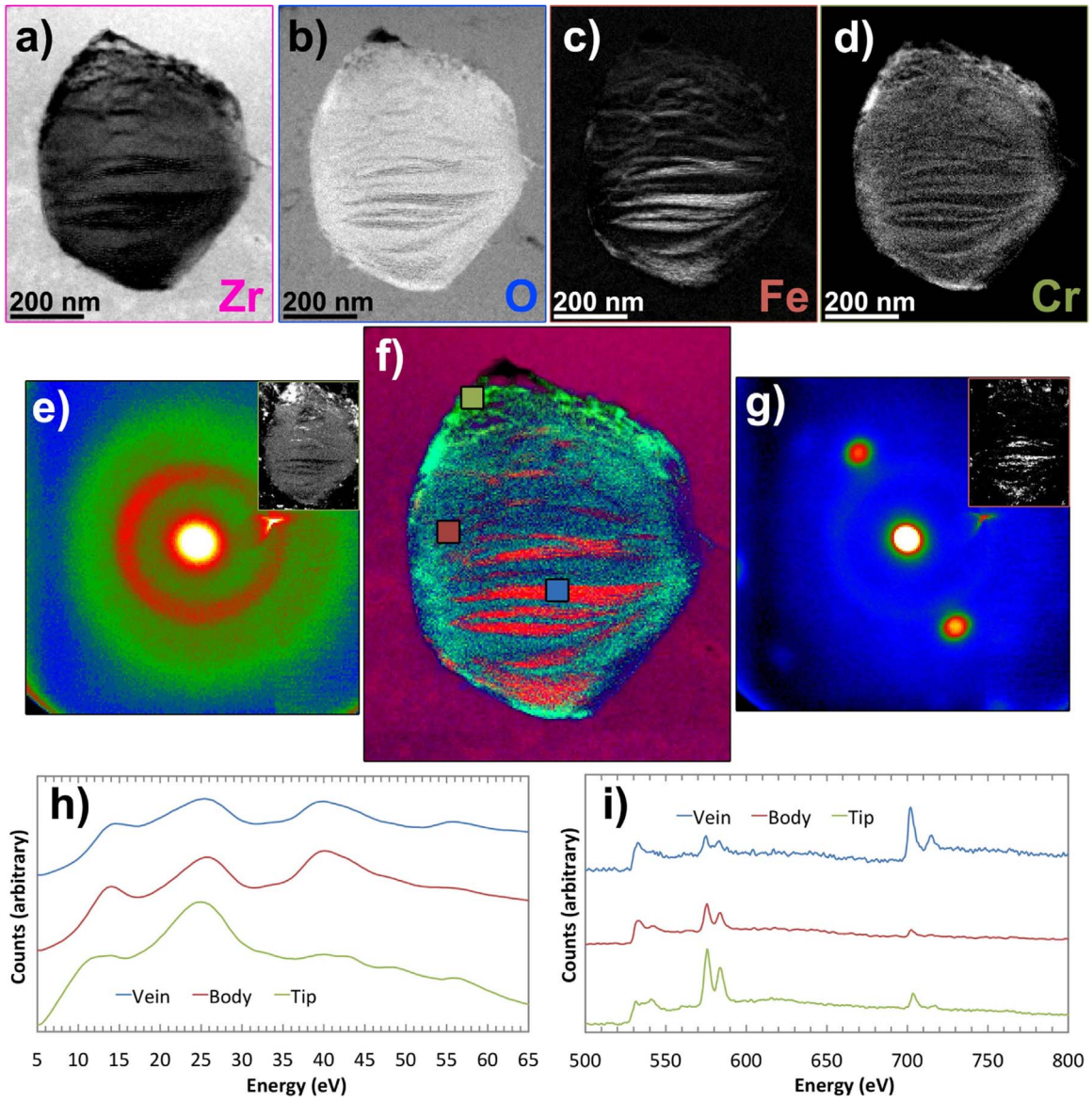

Fig. 5. High-loss quantification of $Zr(Fe, Cr)_2$ precipitate encapsulated by oxide showing; a) map of zirconium areal density; b) map of oxygen areal density; c) map of iron areal density; d) map of chromium areal density; e) scan diffraction image showing diffraction pattern of body of SPP; g) scan diffraction image showing diffraction pattern of Fe-rich veins of SPP and; f) RGB composite of all phases where pink = Zr, blue = O, red = Fe and green = Cr,] with 3 areas highlighted and their corresponding; h) low-loss and; i) high-loss spectral signatures. (For interpretation of the references to colour in this figure legend, the reader is referred to the web version of this article.)

3.5. *Zr(Fe,Cr)$_2$ SPP in oxide*

Fig. 5 shows maps and scanned diffraction from a $Zr(Fe, Cr)_2$ particle ~0.9 μm from the metal:oxide interface of a specimen with a 2.96 μm oxide layer. The structure seen here is totally consistent with the process that was seen as starting in Fig. 4. The segregation of Cr and Fe within the particles has continued to produce the very banded structure shown in Fig. 5a–d and f. As before the majority is a Zr and Cr rich oxide, interspersed with Fe-rich, oxygen-poor bands. As for the other precipitates, cracking can be seen at the tip of this precipitate.

Again, three regions of interest were selected to allow more detailed examination of the spectra, and these areas are highlighted by dots in Fig. 5f, with their corresponding low- and high-loss electron energy loss spectra shown in Fig. 5h and i, respectively.

The region highlighted in blue in Fig. 5f (region 1 in Fig. 5h and i) selected only the contributions to the data set coming from the Fe-rich banding and the low- and high-loss spectral signatures of the bands lying within the SPP shown. Here, the low-loss EEL spectrum shows more of a third peak at lower energy, suggesting some oxidation, but not as strong as in some full oxides shown in Fig. 4f. The high-loss spectrum shows an oxygen K-edge, a weak Cr-$L_{2,3}$ edge, and a strong Fe-$L_{2,3}$ edge. This suggests that the phase is still iron-rich, but contains more oxygen than immediately after the oxidation front passed through, as for the data shown in Fig. 4. Diffraction patterns from the scanned diffraction dataset of such regions all look similar to Fig. 4g, with a strong crystallographic texture, such that there are just slight rotations of this pattern. The spots shown are the 110 reflections of bcc iron, demonstrating that these areas are still principally metallic iron, albeit with more dissolved oxygen content than earlier in the oxidation process

A representative region within the Cr, Zr-rich body of the SPP is shown with a red dot in Fig. 5f which gives the spectra shown region 2 in Fig. 5h and i. This shows an SPP body which is rich in Cr and O (and Zr, not shown in the spectrum), and which is also deficient in Fe. Fig. 5e shows a representative diffraction pattern from a scanned nanodiffraction dataset of the body of the SPP. This mainly displays diffuse rings of intensity at an angle corresponding to a plane spacing of 2.73 Å. This ring is better defined than a typical amorphous diffraction ring, but

the individual spots are difficult to resolve in most cases, suggesting that this material is composed of extremely small nanocrystals, of just a few nm in size. This ring at 2.73 Å could correspond to diffraction from $\{10\bar{1}4\}$ planes in Cr_2O_3 (the strongest reflection from this structure in X-ray diffraction). Thus, the phase could be interpreted as mainly nanocrystalline Cr_2O_3. There are also reflections for monoclinic ZrO_2 in this area, which could also contribute to the ring.

Finally, the region highlighted by a green dot is shown in Fig. 5f (region 3 in Fig. 5h and i) was selected to include only contributions from a Cr-rich 'cap' of the precipitate (note, a Zr-rich cap is seen just above this in Fig. 5a). This region's high-loss spectrum is depleted in Fe, but rich in Cr and O.

All this, is then consistent with the theory that Zr oxidises first, shortly followed by Cr, and that the iron is pushed out of the oxide into separate regions, which never oxidise fully.

4. Discussion

Whilst there have been many previous studies of the oxidation of SPPs in Zircaloys, most studies have left significant unanswered questions. In particular, most studies to date have either performed some imaging and some diffraction, or some imaging and some single point chemical analysis. Performing spatially resolved chemical mapping, and correlating this with the actual crystallographic structure is essential to a complete understanding of what actually happens when SPPs in Zircaloys are oxidised. Of course, the spectroscopic mapping only became possible in recent years, as a result of major technical advances, such as fast DualEELS [35,36]. The scanned diffraction also only became possible in recent years due to modern STEM instruments with the ready achievement of sub-nm, low-convergence angle probes [28] together with suitable CCD cameras and control software.

One of the interesting outcomes of the work is that the oxidation of the rarer Zr_2Fe SPPs is totally different to that of more common Zr $(Cr,Fe)_2$ SPPs. Specifically, the Zr_2Fe SPPs oxidise to form a nanocrystalline precipitate that appears chemically homogeneous down to the 5 nm scale, with a composition corresponding of full oxidation to Fe^{3+} and Zr^{4+}. These precipitates, however, display very strong crystallographic texture and a clear diffraction pattern throughout. The one mystery is that this diffraction pattern does not fit to either a well-known tetragonal ZrO_2 or any known Fe_2O_3 phase but seems to be possible to index to a cubic (or pseudocubic) structure with a lattice parameter close to 4.7 Å. Further work would be needed to elucidate exactly what is going on here.

In contrast to this homogeneity in the oxidation of Zr_2Fe particles, $Zr(Fe, Cr)_2$ oxidation results in huge segregation within the SPP into chromium and zirconium mixed oxide regions and metallic bcc iron regions. It is really quite remarkable that well-crystallised metallic iron is formed as a result of the corrosion process in veins parallel to the corrosion front. Presumably this happens by a mechanism whereby the Zr and Cr are oxidised into some form of mixed oxide, which does not welcome Fe in its structure, thus the Fe diffuses away from the newly formed oxide into the unoxidised part of the SPP. This will gradually enrich in Fe until the concentration is so high that Fe is then precipitated and the crystallite grows rapidly with all the super-saturated Fe at the growth front accreting onto it to form large plate like single crystals. Once the Fe supersaturation has been precipitated, this procedure repeats itself, and this happens multiple times in oxidising a Zr $(Fe, Cr)_2$ SPP. The reader may be wondering why the Fe and Cr do not readily intermix in the oxide form, when Cr_2O_3 and Fe_2O_3 are isostructural (with the hematite/corundum structure). This is, however, well known from previous studies of the oxidation of Fe-Cr-Al alloys, where separate layers of Cr oxides and Fe/Fe oxides are found on the surfaces [37,38]. This is to be expected when one considers the Fe_2O_3-Cr_2O_3 phase diagram [39] where, whilst there is complete solid solubility, significant phase segregation into Fe_2O_3-rich and Cr_2O_3-rich phases would occur under most preparation conditions.

In all cases examined in this paper, cracking can be seen at the edge of SPPs after oxidation. After further examination however, the cracking patterns around Zr_2Fe precipitates are different to those around $Zr(Fe, Cr)_2$ precipitates. Oxidised Zr_2Fe particles typically show lateral cracking in the ZrO_2 to one or other side of the SPP. In contrast to this, $Zr(Fe, Cr)_2$ precipitates typically show cracks at the top (and sometimes the bottom) of the particle. This latter tendency was not just seen in this work, but has also been seen by de Gabory et al. [20,40], Proff et al. [11], and Pêcheur [21]. This difference can easily be explained by strain arguments. As the ratio of the molar volumes of zirconium (Zr) to zirconia (ZrO_2) (denoted the Pilling-Bedworth number) is in the range 1.48–1.56 [41–46], the resulting oxide film must expand on oxidation [47]. This results in the production of a stress gradient across the oxide, which appears at a maximum at the metal:oxide interface and a minimum at the oxide:gas interface [48]. We calculate a Pilling-Bedworth ratio of 1.51 based on published lattice parameters [49,50]. If Zr_2Fe is fully oxidised to a mixture of ZrO_2 and α-Fe_2O_3, this Pilling-Bedworth number would be 1.67 (using α-Fe_2O_3 parameters from [51] and Zr_2Fe parameters from [52]); this number may change slightly for a mixed Zr,Fe oxide, but would likely still exceed 1.51. Seeing as, to a first approximation, oxidation could be seen as a linear process happening along the surface normal direction (and not an isotropic expansion, as suggested by Proff et al. [46], full oxidation of a Zr_2Fe particle would result in the particle being in compressive strain along the growth direction and the surrounding matrix being in tensile strain along that same direction. This would have the effect of opening cracks in the ZrO_2 perpendicular to the growth direction, exactly as observed.

Now for the case of $Zr(Fe, Cr)_2$ SPPs, the volume expansion of full oxidation to a mixture of m-ZrO_2, Cr_2O_3 and α-Fe_2O_3 should give a Pilling-Bedworth ratio of about 1.89 (based on published lattice parameters used above and for Cr_2O_3 from [53]) which would again result in the SPP being in compressive strain and the adjacent ZrO_2 in tensile strain; this is similar to that for pure $ZrCr_2$ of 1.78 [46]. But, these SPPs are not fully oxidised. In fact, our conclusions are that much of the Fe is not oxidised and instead precipitates as metallic bcc iron. When this is taken into account, the Pilling-Bedworth ratio is much smaller, just 1.53 for all iron remaining as metal and all Zr and Cr being fully oxidised (using lattice parameters for alpha iron from [54]). This would be close enough to the 1.51 for ZrO_2 such that stress and cracking would be minimal. But, if some of the Cr was also unoxidised (e.g. dissolved in the ferrite), the Pilling-Bedworth ratio would be smaller than 1.53 and the SPP would not quite fill the void created by the oxidation of the surrounding Zr. This is exactly what is observed where small voids or cracks are typically seen at the outer tip of such oxidised Laves phase SPPs. It is also true that differences in thermal expansion could contribute to such void formation, although this has not been calculated here as that would be a more complex calculation requiring detailed knowledge of the thermal expansion behaviour of all phases involved. Nevertheless, it is believed that thermal expansion mismatches would have a minimal effect [46].

This clearly demonstrates therefore, that Zr_2Fe SPPs will inevitably result in cracking of the oxide scale due to the expansion mismatch with the Zr matrix on oxidation. Since Zr_2Fe is only believed to form at higher iron content [7], it may be that this effect could be reduced by reducing iron content somewhat. Indeed, this could be one reason why Charquet [7] found a worse corrosion resistance for high Fe:Cr ratios in Zircaloy. This happens in addition to any cracking that appears due to mechanical mismatches resulting from the undulation of the metal-oxide interface [55].

The formation of small voids above partially oxidised $Zr(Cr,Fe)_2$ Laves-phase SPPs is probably similar to the formation of crescent shaped cracking above unoxidised SPPs in the oxide layer of Zr1%Cr samples [11] and in unoxidised or partially oxidised SPPs in other studies. This is probably less significant for the formation of connected cracking, as they are generally just some free space at the SPP imposing no tensile strain on the zirconia scale.

5. Conclusions

Coupled STEM imaging, DualEELS and scanned diffraction has been used to provide a comprehensive study of the oxidation of SPPs in Zircaloy-4 during corrosion in superheated water. Two main forms of SPP are found, the frequently observed Zr(Fe, Cr)$_2$ Laves-phase type, as well as some Zr_2Fe particles (isostructural with Zr_2Ni).

Zr_2Fe precipitates begin as fairly round, homogenous precipitates within the metal matrix, and oxidise in a fairly uniform manner, to a nanocrystalline, fully oxidised $Fe^{3+}Zr^{4+}$ mixed oxide. There is a strong crystallographic texture developed in oxidation, but the crystalline phase was unidentified and neither matches tetragonal ZrO_2 nor any known phase of Fe_2O_3. Instead, the diffraction pattern was consistent with a ⟨114⟩ pattern of a cubic structure with a lattice parameter ~4.7 Å.

Zr(Fe, Cr)$_2$ precipitates begin as very faceted structures within the metal matrix, with O enrichment of the outside rim. Fe concentration is also seen to increase in specific areas within the centre of precipitates. Such SPPs develop into a more elongated shape upon oxidation, with a strongly banded elemental segregation. There are three phases found: i) a Cr rich cap which we presume to be Cr_2O_3 with some Fe substitution; ii) a Zr, Cr nanocrystalline oxide body with an approximate 3:2 ratio of Zr:Cr, and very little Fe content. The diffraction pattern reveals a ring pattern of randomly oriented nanocrystallites, with a ring consistent with some reflections of either Cr_2O_3 or monoclinic ZrO_2 or a mixture of the two; iii) veins of well-crystallised metallic α-Fe with low oxygen content, with a strong texture mostly running parallel to the metal-oxide interface.

The Zr_2Fe precipitates cause cracking in the vicinity because the expansion on oxidation is larger than for the Zr → ZrO_2 reaction putting the ZrO_2 either side into tensile strain. On the other hand the Zr(Fe, Cr)$_2$ can leave small voids or cracks at the upper tip due to the incomplete oxidation of the iron which results in less expansion of the SPP than the Zr → ZrO_2. Providing an understanding of the corrosion process of SPPs within Zircaloys such as has been presented in this work, which can provide elemental distribution, valence state and crystal structure, gives an understanding beyond that previously obtained on the complex corrosion that takes place. This may also provide some information on the possible influence of SPPs on the overall corrosion behaviour of Zircaloy-4 in simulated reactor conditions.

Acknowledgements

IM and KJA are grateful to Amec Foster Wheeler for funding this work and to Amec Foster Wheeler and the EPSRC for the provision of a PhD studentship to KJA. This work would not have been possible without the provision of the MagTEM microscope facility by SUPA and the University of Glasgow. We are grateful to Dr Paul Thomas of Gatan UK Ltd. for helpful discussions on EELS quantification using DualEELS and the provision of experimental plug-ins for Digital Micrograph, together with prompt responses to technical questions and bug reports. IM is also indebted to Prof. Alan J. Craven for his many helpful suggestions and discussions regarding EELS theory and data processing.

References

[1] B. Cox, Some thoughts on the mechanisms of in-reactor corrosion of zirconium alloys, J. Nucl. Mater. 336 (2–3) (2005) 331–368.
[2] S. Nakamura, H. Harada, S. Raman, P.E. Koehler, Thermal neutron capture cross sections of zirconium-91 and zirconium-93 by prompt γ-ray spectroscopy, J. Nucl. Sci. Technol. 44 (1) (2007) 21–28.
[3] B. Cox, The oxidation and corrosion of zirconium and its alloys: V. mechanism of oxide film growth and Breakdown on zirconium and zircaloy-2, J. Electrochem. Soc. 108 (1) (1961) 24–30.
[4] N. Ni, S. Lozano-Perez, J. Sykes, C. Grovenor, Quantitative EELS analysis of zirconium alloy metal/oxide interfaces, Ultramicroscopy 111 (2) (2011) 123–130.
[5] A. Garner, A. Gholinia, P. Frankel, M. Gass, I. MacLaren, M. Preuss, The microstructure and microtexture of zirconium oxide films studied by transmission electron backscatter diffraction and automated crystal orientation mapping with transmission electron microscopy, Acta Mater. 80 (2014) 159–171.
[6] J. Hu, A. Garner, N. Ni, A. Gholinia, R. Nicholls, S. Lozano-Perez, P. Frankel, M. Preuss, C. Grovenor, Identifying suboxide grains at the metal-oxide interface of a corroded Zr-1.0%Nb alloy using (S)TEM, transmission-EBSD and EELS, Micron (2014).
[7] D. Charquet, Improvement of the uniform corrosion resistance of Zircaloy-4 in the absence of irradiation, J. Nucl. Mater. 160 (2–3) (1988) 186–195.
[8] A. Yilmazbayhan, O. Delaire, A.T. Motta, R.C. Birtcher, J.M. Maser, B. Lai, Determination of the alloying content in the matrix of Zr alloys using synchrotron radiation microprobe X-ray fluorescence, J. Nucl. Mater. 321 (2) (2003) 221–232.
[9] Z.G. Zhang, Z.H. Feng, X.J. Jiang, X.Y. Zhang, M.Z. Ma, R.P. Liu, Microstructure and tensile properties of novel Zr–Cr binary alloys processed by hot rolling, Mater. Sci. Eng.: A 652 (2016) 77–83.
[10] K. Ali, A. Arya, P.S. Ghosh, G.K. Dey, A first principles study of cohesive, elastic and electronic properties of binary Fe–Zr intermetallics, Comput. Mater. Sci 112 (2016) 52–66.
[11] C. Proff, S. Abolhassani, C. Lemaignan, Oxidation behaviour of binary zirconium alloys containing intermetallic precipitates, J. Nucl. Mater. 416 (1–2) (2011) 125–134.
[12] P. Chemelle, D.B. Knorr, J.B. Van Der Sande, R.M. Pelloux, Morphology and composition of second phase particles in zircaloy-2, J. Nucl. Mater. 113 (1) (1983) 58–64.
[13] X. Meng, D.O. Northwood, Second phase particles in Zircaloy-2, J. Nucl. Mater. 168 (1) (1989) 125–136.
[14] B. Hutchinson, B. Lehtinen, A theory of the resistance of Zircaloy to uniform corrosion, J. Nucl. Mater. 217 (3) (1994) 243–249.
[15] C. Degueldre, J. Raabe, G. Kuri, S. Abolhassani, Zircaloy-2 secondary phase precipitate analysis by X-ray microspectroscopy, Talanta 75 (2) (2008) 402–406.
[16] J.P. Gros, J.F. Wadier, Precipitate growth kinetics in Zircaloy-4, J. Nucl. Mater. 172 (1) (1990) 85–96.
[17] D. Pêcheur, F. Lefebvre, A.T. Motta, C. Lemaignan, J.F. Wadier, Precipitate evolution in the Zircaloy-4 oxide layer, J. Nucl. Mater. 189 (3) (1992) 318–332.
[18] Y. Hatano, R. Hitaka, M. Sugisaki, M. Hayashi, Influence of size distribution of Zr (Fe, Cr)2 precipitates on hydrogen transport through oxide film of Zircaloy-4, J. Nucl. Mater. 248 (0) (1997) 311–314.
[19] C. Toffolon-Masclet, J.-C. Brachet, G. Jago, Studies of second phase particles in different zirconium alloys using extractive carbon replica and an electrolytic anodic dissolution procedure, J. Nucl. Mater. 305 (2–3) (2002) 224–231.
[20] B. de Gabory, A.T. Motta, K. Wang, Transmission electron microscopy characterization of Zircaloy-4 and ZIRLO™ oxide layers, J. Nucl. Mater. 456 (2015) 272–280.
[21] C. Toffolon-Masclet, T. Guilbert, J.C. Brachet, Study of secondary intermetallic phase precipitation/dissolution in Zr alloys by high temperature–high sensitivity calorimetry, J. Nucl. Mater. 372 (2) (2008) 367–378.
[22] D. Fuloria, N. Kumar, S. Goel, R. Jayaganthan, S. Jha, D. Srivastava, Tensile properties and microstructural evolution of Zircaloy-4 processed through rolling at different temperatures, Mater. Des. 103 (2016) 40–51.
[23] H.S.F. Garzarolli, Behaviour of structural materials for fuel and control elements in light water cooled power reactors, Proc. IAEA Int, Symp. Improv. Water Reactor Technol. Util. (1986).
[24] D. Pêcheur, Oxidation of β-Nb and Zr(Fe, V)2 precipitates in oxide films formed on advanced Zr-based alloys, J. Nucl. Mater. 278 (2–3) (2000) 195–201.
[25] D. Charquet, Influence of precipitates on the corrosion of Zircaloy-4 in 400 °C steam, J. Nucl. Mater. 211 (3) (1994) 259–261.
[26] T. Couvant, Corrosion in pressurized water reactors (PWRs), in: K.L. Murty (Ed.), Materials Ageing and Degradation in Light Water Reactors, Woodhead Publishing, 2013, pp. 70–80.
[27] M. Le Calvar, I. De Curières, Corrosion issues in pressurized water reactor (PWR) systems, in: D. Féron (Ed.), Nuclear Corrosion Science and Engineering, Woodhead Publishing, 2012, pp. 473–547.
[28] S. McVitie, D. McGrouther, S. McFadzean, D.A. MacLaren, K.J. O'Shea, M.J. Benitez, Aberration corrected Lorentz scanning transmission electron microscopy, Ultramicroscopy 152 (2015) 57–62.
[29] J. Bobynko, I. MacLaren, A.J. Craven, Spectrum imaging of complex nanostructures using DualEELS: I. digital extraction replicas, Ultramicroscopy 149 (0) (2015) 9–20.
[30] K.J. Annand, I. MacLaren, M. Gass, Utilising DualEELS to probe the nanoscale mechanisms of the corrosion of Zircaloy-4 in 350 °C pressurised water, J. Nucl. Mater. 465 (2015) 390–399.
[31] R.F. Egerton, Oscillator-strength parameterization of inner-shell cross sections, Ultramicroscopy 50 (1) (1993) 13–28.
[32] J.A. Navío, M.C. Hidalgo, G. Colón, S.G. Botta, M.I. Litter, Preparation and physicochemical properties of ZrO2 and Fe/ZrO2 prepared by a sol-Gel technique, Langmuir 17 (1) (2001) 202–210.
[33] L. Chen, J. Hu, R.M. Richards, Catalytic properties of nanoscale iron-Doped zirconia solid-Solution aerogels, Chem. Phys. Chem 9 (7) (2008) 1069–1078.
[34] Z.L. Wang, Valence electron excitations and plasmon oscillations in thin films, surfaces, interfaces and small particles, Micron 27 (3) (1996) 265–299.
[35] J. Scott, P.J. Thomas, M. MacKenzie, S. McFadzean, J. Wilbrink, A.J. Craven, W.A.P. Nicholson, Near-simultaneous dual energy range EELS spectrum imaging, Ultramicroscopy 108 (12) (2008) 1586–1594.
[36] A. Gubbens, M. Barfels, C. Trevor, R. Twesten, P. Mooney, P. Thomas, N. Menon, B. Kraus, C. Mao, B. McGinn, The GIF Quantum, a next generation post-column imaging energy filter, Ultramicroscopy 110 (8) (2010) 962–970.
[37] H. Götlind, F. Liu, J.-E. Svensson, M. Halvarsson, L.-G. Johansson, The effect of water vapor on the initial stages of oxidation of the FeCrAl alloy kanthal AF at 900 °C, Oxid. Met. 67 (5) (2007) 251–266.

[38] E. Airiskallio, E. Nurmi, M.H. Heinonen, I.J. Väyrynen, K. Kokko, M. Ropo, M.P.J. Punkkinen, H. Pitkänen, M. Alatalo, J. Kollár, B. Johansson, L. Vitos, High temperature oxidation of Fe–Al and Fe–Cr–Al alloys: the role of Cr as a chemically active element, Corros. Sci. 52 (10) (2010) 3394–3404.
[39] A. Muan, S. Somiya, Phase equilibria in the system iron oxide—Cr2O3–SiO2 in air, J. Am. Ceram. Soc. 43 (10) (1960) 531–541.
[40] A.T.M.B. de Gabory, Structure of zircaloy 4 oxides formed during autoclave corrosion, ANS LWR Fuel Performance Meeting, TopFuel, Charlotte, NC, September 2013, 2013.
[41] R. Bedworth, N. Pilling, The oxidation of metals at high temperatures, J. Inst. Met. 29 (3) (1923) 529–582.
[42] T. Arima, K. Miyata, Y. Inagaki, K. Idemitsu, Oxidation properties of Zr–Nb alloys at 500–600 °C under low oxygen potentials, Corros. Sci. 47 (2) (2005) 435–446.
[43] Z.J. Zhu, M.Y. Yao, X.D. Xue, Y.C. Wu, B.X. Zhou, Corrosion-related defects in Zircaloys: a preliminary study with slow positron beam, J. Phys.: Conf. Ser. 505 (1) (2014) 012008.
[44] J. Wei, P. Frankel, M. Blat, A. Ambard, R. Comstock, L. Hallstadius, S. Lyon, R. Cottis, M. Preuss, Autoclave study of zirconium alloys with and without hydride rim, Corros. Eng. Sci. Technol. 47 (7) (2012) 516–528.
[45] C. Roy, B. Burgess, A study of the stresses generated in zirconia films during the oxidation of zirconium alloys, Oxid. Met. 2 (3) (1970) 235–261.
[46] C. Proff, S. Abolhassani, C. Lemaignan, Oxidation behaviour of zirconium alloys and their precipitates – a mechanistic study, J. Nucl. Mater. 432 (1) (2013) 222–238.
[47] J.P. Pemsler, Diffusion of oxygen in zirconium and its relation to oxidation and corrosion, J. Electrochem. Soc. 105 (6) (1958) 315–322.
[48] V.Y. Gertsman, A.P. Zhilyaev, J.A. Szpunar, Grain boundary misorientation distributions in monoclinic zirconia, Modell. Simul. Mater. Sci. Eng. 5 (1) (1997) 35.
[49] R.J. Hill, L.M.D. Cranswick, International-union-of-crystallography – commission-on-powder-diffraction – rietveld refinement round-robin. 2. Analysis of monoclinic zro2, J. Appl. Crystallogr. 27 (1994) 802–844.
[50] J. Goldak, L.T. Lloyd, C.S. Barrett, Lattice Parameters, Thermal Expansions, and Gruneisen Coefficients of Zirconium, 4. 2–1130, Phys. Rev. 144 (2) (1966) 478–484.
[51] Maslen, Acta Crystallographica Section B: Structural Science (50) (1994) 435–441.
[52] T.O. Malakhova, Z.M. Alekseyeva, The Zr-Fe phase diagram in the range 20–40 at.% Fe and the crystalline structure of the intermetallic compound Zr3Fe, J. Less Common Met. 81 (2) (1981) 293–300.
[53] E.L. Belokoneva, Zh. Neorg. Khim. 48 (2003) 960–968.
[54] M.E. Straumanis, D.C. Kim, Z. fuer Metallkunde 60 (1969) 272–277.
[55] E. Polatidis, P. Frankel, J. Wei, M. Klaus, R.J. Comstock, A. Ambard, S. Lyon, R.A. Cottis, M. Preuss, Residual stresses and tetragonal phase fraction characterisation of corrosion tested Zircaloy-4 using energy dispersive synchrotron X-ray diffraction, J. Nucl. Mater. 432 (1–3) (2013) 102–112.